Optimal Design of a Five-phase External Rotor Permanent Magnet Machine for Convey Application

F. Tan, J. Gong, Q. Zhao, H. Wang, N-k. Nguyen, E. Semail, N. Bracikowski, F. Gillon

***Abstract* -- This paper proposes the design and development of a five-phase external rotor permanent magnet synchronous machine (PMSM) which is used for direct drive convey application. Firstly, the slot/pole combination of fraction slot concentrated winding (FSCW) is selected according to three criteria; secondly, the analytical model of the proposed machine topology is built and optimized, the initial machine parameters are then obtained; thirdly, the machine is optimized by combing the finite element model and the Kriging model, and the final optimal results are compared to the initial one. Detail design principles and performance characteristics of the proposed machine topology are presented and validated with finite element models.**

***Index Terms*—Five-phase machine, external rotor, permanent magnet, convey application.**

I. INTRODUCTION

WITH redundant design in machine phases, multiphase machines (>3 phases) are essentially characterized with high reliability which makes them widely used in in critical applications, such as historically marine electric propulsion [1], aerospace [2] and automotive traction [3], with multiphase machines supplied by a voltage source inverter. Compared to classical wye-coupled three-phase machines, which possess the minimum number of independent currents for achieving a rotating field in normal condition, multiphase machines have more degrees of freedom than the minimum necessary, thus allowing a rotating field even with one opened phase.

In the context of high reliability requirement, this paper proposes and develops an external five-phase PMSM. The design adopts fractional-slot concentrated winding which is characterized by short end windings, high power density, high efficiency, high slot-filling factor, small cogging torque, etc. [4-6]. Therefore, the proposed machine can be benefits with high power, high torque and high efficiency capability.

The paper will be organized as follows. After a brief introduction about the multiphase machine, the selection of the proposed machine topology is presented in section II. The analytical model is built, and optimization problem is formulated and optimized in section III. Based on the initial design obtained in section II, a finite element model (FEM) is constructed and optimized by combining a Kriging model in section IV. The performance of the proposed machine is analyzed using FEM in section V.

F. Tan, J. Gong are with the School of Electrical Engineering, Shandong University, Jinan, 250061, China (e-mail: gongjinlin@sdu.edu.cn).

H. Wang, Q. Zhao are with the Excellent Electric Co. Ltd., Shandong Province, Jining City 272000, China.

N-k. Nguyen, E. Semail, F. Gillon are with Univ. Lille, Arts et Métiers ParisTech, Centrale Lille, HEI, EA 2697-L2EP-Laboratoire d'Electrotechnique et d'Electronique de Puissance, F-59000 Lille, France.

N. Bracikowski is with IREENA University of Nantes, 44600 Saint-Nazaire, France.

II. MOTOR TOPOLOGY

For the direct drive convey application, the external rotor structure with surface mounted permanent magnet is choosed due to the high torque density. The selection of the slot/pole combination is the first step for the design of machine. The relationship between the number of slots and the number of poles for a 5-phase machine should be respected as follows [7]:

$$\frac{N_s}{GCD\{N_s, 2p\}} = 5k \tag{1}$$

Where N_s is the number of slots, GCD is the greatest common multiple, p is the number of poles, and k is an integer.

A. LCM and GCD

Greatest common divisor (GCD) and least common multiple (LCM) of the slot/pole combination are firstly taken into account. The larger the value of the GCD, the smaller the torque ripple [8]; and the larger the LCM, the smaller the noise and vibration. TABLE I lists the different combinations of the slots and poles for 5-phase machines. The former number is GCD, the latter number is LCM.

TABLE I
SLOT/POLE NUMBER SELECTION

poles \ slots	30	40	50
28	2-420	4-280	2-700
30			10-150
32	2-480	8-160	2-800
34	2-510	2-680	2-850
36	6-180	4-360	2-900
38	2-570	2-760	2-950
40			10-200
42	6-210	2-840	2-1050
44	2-660	4-440	2-1100
46	2-690	2-920	2-1150
48	6-240	8-240	2-1200
50	10-150		
52	2-780	4-520	2-1300

It can be noted that, the families have been sorted by background color in TABLE I. Orange family exhibits low LCD, and blue family is with low LCM. The one in black is not feasible, and the red values represent the high LCM and GCD, i.e. potential candidates.

B. Winding factor

The Winding factor of high value is also an important parameter which is related to the torque density. The windings factors of the three candidates selected in part A are calculated and shown in TABLE II.

TABLE II
WINDING FACTOR COMPARISON

Slot pole number combination / winding factor	40*s*/36*p*	40*s*/44*p*	40*s*/52*p*
k_{w1}	0.976	0.976	0.880
k_{w3}	0.794	0.794	0.139

In which, k_{w1} represents the fundamental winding factor, and k_{w3} represents the third harmonic winding factor which is also considered due to the specialty of multiphase machines. As can be seen from the Table II, 40*s*/36*p*, 40*s*/44*p* have higher winding factors which will be taken as candidates for further study.

C. MMF distribution

The mmf spectrum of the last two candidates are shown in Fig. 1. It can be seen that the same spectrum is obtained. However, the working harmonic is the 18th and the 22th respectively. It should be noted that the small value of the thickness of the back-iron can be designed with bigger value of poles.

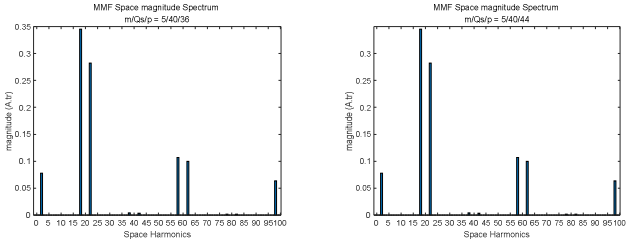

(a) 40s/36p machine (b) 40s/44p machine

Fig.1. mmf spectrum of two candidates

Considering the above three criteria, the 40-slot/44-pole combination is finally selected for further design.

III. MOTOR DESIGN AND OPTIMIZATION

A. Modeling process

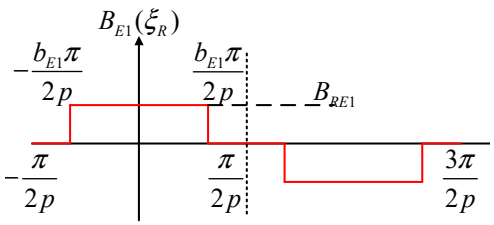

Fig. 2. Air gap flux density waveform

First determine the magnetic density of the motor, which is the basis of the motor design parameters and radial dimensions are all obtained from the magnetic density.

Fig. 2 is the air gap flux density waveform. ξ_R is the mechanical angle in the rotor coordinate system, b_{E1} is the pole arc coefficient, B_{RE1} is the air gap magnetic density amplitude. Combined with Fig. 2, the expression of the air-gap flux density B_{E1} is as follows:

$$B_{E1}(\xi_S,\theta)=\frac{4B_{RE1}}{\pi}\sum_{i=0}^{\infty}\frac{1}{h}\sin\left(h\frac{b_{E1}\pi}{2}\right)\cos\left(hp(\xi_S-\theta)\right) \tag{2}$$

$$h=2i+1,\ \xi_S=\xi_R+\theta \tag{3}$$

Where ξ_S is the mechanical angle in the stator coordinate system, θ is the rotor position angle.

According to (2) (3), the expression of the magnetic flux of one turn of the coil $\Phi(\theta)$ can then be obtained:

$$\Phi(\theta)=\frac{8k_pB_{RE1}}{\pi p}R_3l\sum_{i=0}^{\infty}\frac{\sin(h\frac{\pi}{2})}{h^2}\sin(h\frac{b_{E1}\pi}{2})\cos(hp\theta) \tag{4}$$

Where k_p is the pitch factor, l is the axial length of the motor, R_3 is the average radius of the air gap, which is signed in the Fig. 3.

R_3 : the average radius of the air gap.
R_1 : the radius at the bottom of the stator slot.
L_{AE} : Permanent magnet thickness.
L_{tooth} : tooth width.
L_{CSE} : Stator yoke thickness.
L_{CRE} : Rotor yoke thickness.
L_E : Slot depth.
L_{ts} : Tooth shoe length.

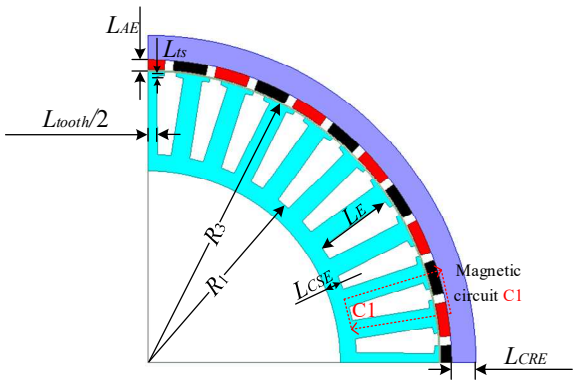

Fig. 3. Motor radial dimension drawing

According to (4), the expression of the magnetic flux of each phase $\Phi_{ph}(\theta)$ can be obtained:

$$\Phi_{ph}(\theta)=\frac{16k_wN_sB_{RE1}}{\pi}R_3l\sum_{i=0}^{\infty}\frac{\sin(h\frac{\pi}{2})}{h^2}\sin(h\frac{b_{E1}\pi}{2})\cos(hp\theta) \tag{5}$$

According to (5), the electromotive force $e(t)$ can be expressed:

$$e(t)=\frac{16k_wN_s\omega B_{RE1}}{\pi}R_3l\sum_{i=0}^{\infty}\frac{\sin(h\frac{\pi}{2})}{h}\sin(h\frac{b_{E1}\pi}{2})\sin(h\omega t) \tag{6}$$

Motor design adopts virtual motor design. Each virtual two-phase motor corresponds to a set of harmonics. The torque of a five-phase motor T_{em} can be expressed as:

$$T_{em} = \frac{E_1}{\omega}\frac{\pi}{2N_s}K_F AR_1 \tag{7}$$

$$K_F = \frac{1+K_E K_I}{\sqrt{1+K_I^2}} \tag{8}$$

$$K_E = \frac{E_1}{E_3}, K_I = \frac{I_1}{I_3} \tag{9}$$

Where E_n is the rms value of the n^{th} harmonic of EMF, and I_n is the rms value of the n^{th} harmonic of the injected current. A is the line load.

Substituting (6) into (7), the torque expression T_{em} can be rewritten as:

$$T_{em} = \frac{8k_{w1}}{\sqrt{2}}B_{RE1}\sin(\frac{b_{E1}\pi}{2})K_F AR_1R_3 l \tag{10}$$

B. Determination of the working point of PM

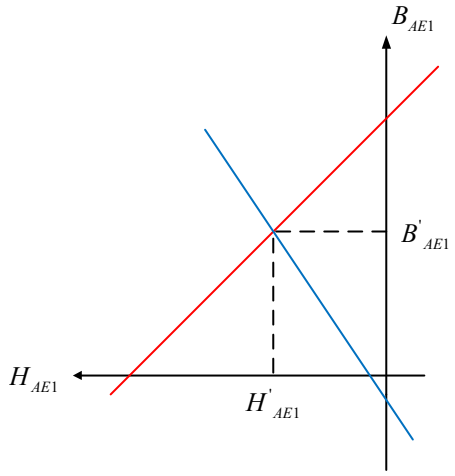

Fig. 4. The working point of the permanent magnet
*Blue is the load line. Red is the characteristic line

Fig. 4 is the working point of the permanent magnet, which is the intersection of the load line and the characteristic line of the permanent magnet.

According to Ampere's loop theorem(C1 is signed in Fig. 3), assuming that all the magnetic flux of the permanent magnet enter the air gap and the stator and there is no magnetic leakage, the thickness of the permanent magnet L_{AE} is obtained as:

$$L_{AE} = \frac{B'_{AE}\mu_{RME}K_{KE}e}{J_{RME}-B'_{AE}} + \frac{\mu_{RME}}{2(J_{RME}-B'_{AE})}(\frac{B_{ROT}L_{ROT}}{\mu_{ROT}}+\frac{B_{STA}L_{STA}}{\mu_{STA}}+\frac{2B_tL_E}{\mu_t}) \tag{11}$$

Where J_{RME} is the remanence of the permanent magnet. e is the air gap length. B_{ROT} , B_{STA} and B_t are the magnetic densities of rotor yoke, stator yoke and teeth respectively. L_{ROT} , L_{STA} and L_E are the magnetic path length of rotor yoke, stator yoke and teeth respectively. μ_{RME}, μ_{ROT}, μ_{STA}, μ_t are the relative permeability of permanent magnet, rotor yoke, stator yoke and teeth respectively. K_{KE} is Carter coefficient, which is affected by the shape of the slot.

As long as the magnetic density and torque of the motor are known, the radial size of the motor can be obtained. Therefore, the inverse model of the motor can be derived according to the direct model, so as to prepare for the optimization of the motor.

C. Analytical Model Optimization

Fmincon is a matlab function for solving the minimum value of nonlinear multivariate functions. According to the principle of motor design, taking the maximum torque as the optimization goal, the motor design parameters are optimized. The optimization conditions are as follows:

$$\begin{cases} \min\limits_{L_{CSE},L_{CRE},L_E,L_{AE},L_{tooth}} \{-f\} \\ \text{s.t.} \quad B_{RE1} \le 1.0,\ B_{STA} \le 1.5,\ B_t \le 1.732 \end{cases} \tag{12}$$

with

$$L_{CSE} \in [25,45], L_E \in [60,120], L_{AE} \in [8,15], L_{tooth} \in [20,30]$$
$$f = T_{em} \tag{13}$$

According to (12) (13), The optimization problem contains one objective function and three constraint functions, the purpose is to get the maximum torque as possible. At the same time, magnetic density must be limited.

After the optimization of the fmincon function, the initial motor parameter values can be obtained in TABLE III. On the basis of these initial values, the variable range is further narrowed, and then the Kriging proxy model is optimized.

D. Kriging model Optimization

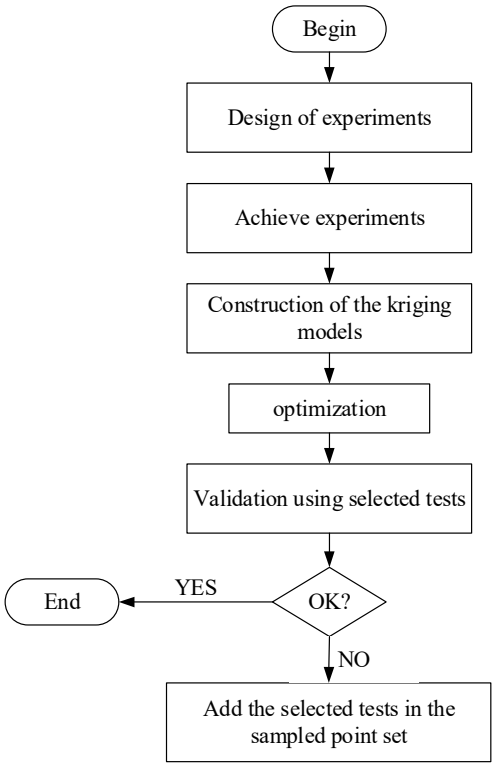

Fig. 5. Kriging Model Optimization Flowchart

Kriging model is an interpolation method for optimal linear unbiased estimation of spatially distributed data. It can estimate the error distribution of the model, has strong local refinement ability, and is suitable for highly nonlinear responses. It is based on finite element model analysis, which can greatly shorten the time period of finite element calculation and improve work efficiency [9], The flowchart of kriging model Optimization as shown in Fig. 5.

In the case, firstly, 100 sample points are selected for finite element analysis, and these 100 sample points are selected by the Latin hypercube method. After the simulation of 100 sample points, it is substituted into the model. According to the evaluation value of the finite element model, an initial model is established for each objective function and constraint function, and the pareto optimal solution set is finally obtained, so as to obtain the optimal solution for motor optimization.

The kriging model optimization results are shown in TABLE III.

TABLE III
OPTIMIZATION RESULTS OF FMINCON FUNCTION AND KRIGING ,MODEL

parameter	Fmincon value	Kriging vaule
Stator diameter(mm)	723.4	719
Rotor diameter(mm)	810	810
Active length(mm)	684	684
Airgap length(mm)	2.5	2.5
PM thickness(mm)	10.8	13
PM height(mm)	684	684
Slot height(mm)	97.7	95.7

IV. PERFORMANCE ANALYSIS

A. *No-Load Analysis*

The final design of kriging model optimization results in the Table III is analyzed using FEM. Fig. 6 shows the 1/2 structure of the design, and the magnetic field line and the magnetic density are obtained by FE method. In the context of the direct drive convey application, there exists a mechanical constraint on the thickness of the rotor back-iron, which has been taken into account during the design step. It explains the lower value of the flux density in the rotor back-iron.

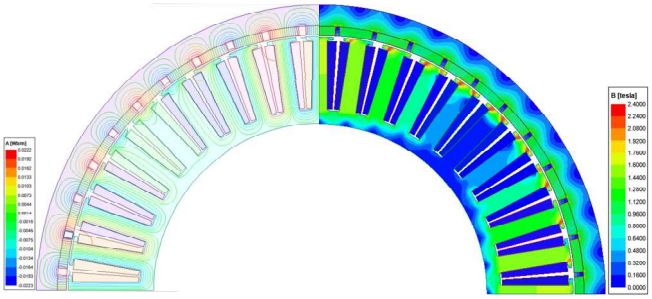

Fig. 6. magnetic field distribution under no-load condition

Cogging torque is the torque generated by the interaction between the permanent magnet and the stator teeth, which can influence the quality of the output torque and thus cause vibration of the drive system. It is desired to as small as possible and is taken into account within design step. Fig. 7 shows the cogging torque waveform.

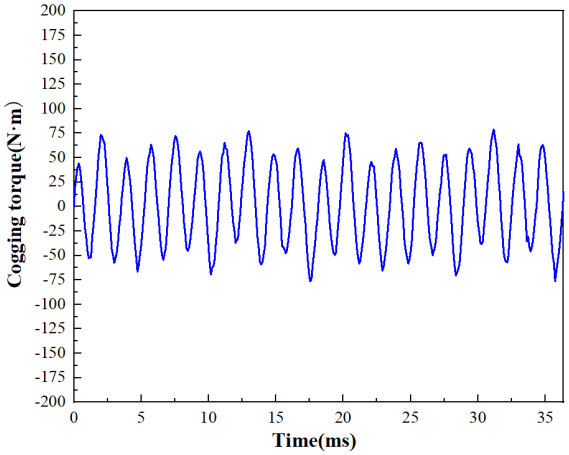

Fig. 7. The cogging torque waveform.

It can be seen from the Fig. 7 that the maximum cogging torque is about 80 N·m, which is about 0.39% of the average output torque.

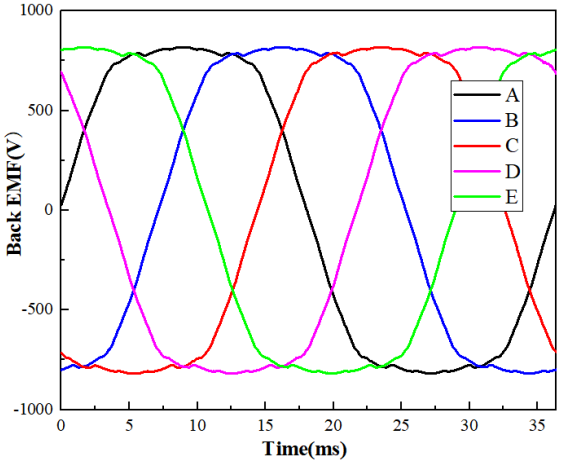

Fig. 8. The no-load back EMF waveform.

The no-load trapezoidal back-EMF waveform and its spectrum are shown in Fig. 8 and Fig. 9 respectively. It can be seen from Fig. 9 that the amplitude of the fundamental harmonic is about 930V, and the amplitude of the 3rd harmonic is about 135V, the other harmonics are negligible.

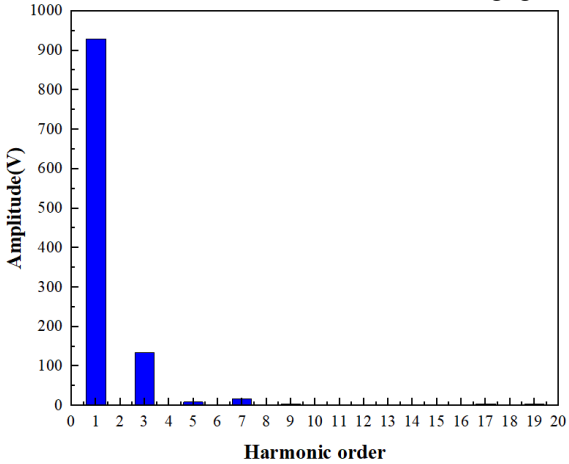

Fig. 9. Fourier decomposition of the no-load back EMF of phase A

B. *On-Load Analysis*

The torque characteristics are evaluated under two kinds of supply: with the first only or both first and third sinusoidal currents as shown in Fig. 10. The amplitude values of the two kinds current supply are kept the same and injected with MTPA control strategy.

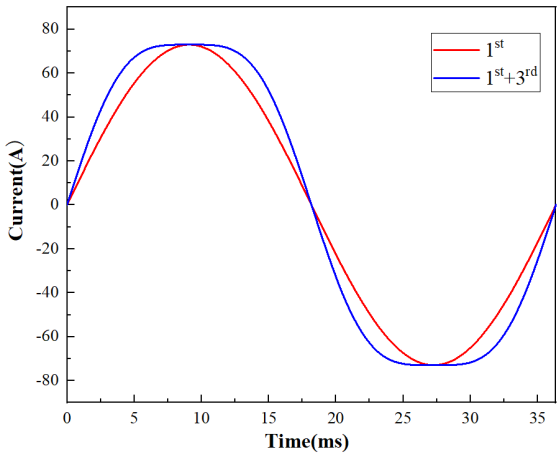

Fig. 10. The two kinds current supply

Fig. 11 shows the wave forms of the torques at the speed 75 rpm. As expected, the torque with the two harmonic current injection (1^{st} + 3^{rd}) is 11.8% higher than the one obtained with only the 1^{st} harmonic current. It can be observed that the torque ripples are only 1.01% and 1.33%, respectively.

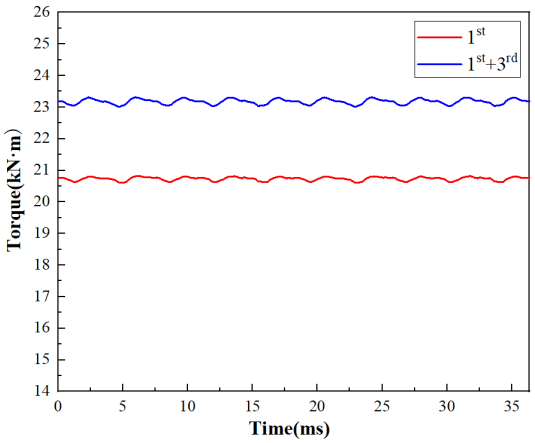

Fig. 11. The wave forms of the torques

V. CONCLUSION

This paper presents the design and development of a five-phase PMSM with external rotor structure for direct convey application. The 5-phase/40-slot/44-pole topology of FSCW is firstly selected according to three criteria: torque ripple, winding factor and mmf distribution. Then, the analytical model of the proposed structure is built and the initial design is obtained using optimization process. The FEM of the initial design is constructed and optimized by integrating a Kriging model. The performances of the final optimized design are shown based on the FE analysis. A prototype is producing and all the analysis will be compared to the experiment results in the final paper.

VI. REFERENCES

[1] Z. Zhang, S. Yu, F. Zhang, S. Jin, and X. Wang, "Electromagnetic and Structural Design of a Novel Low-Speed High-Torque Motor With Dual-Stator and PM-Reluctance Rotor," IEEE T. Appl. Supercon., vol. 30, no. 4, pp. 1-5. 2020.

[2] T. Zhao, S. Wu, and S. Cui, "Multiphase PMSM With Asymmetric Windings for More Electric Aircraft," IEEE Transactions on Transportation Electrification, vol. 6, no. 4, pp. 1592-1602. 2020.

[3] Y. Yang, M. M. Rahman, T. Lambert, B. Bilgin, and A. Emadi, "Development of an External Rotor V-Shape Permanent Magnet Machine for E-Bike Application," IEEE T. Energy Conver., vol. 33, no. 4, pp. 1650-1658. 2018.

[4] M. Farshadnia, M. A. Masood Cheema, A. Pouramin, R. Dutta, and J. E. Fletcher, "Design of Optimal Winding Configurations for Symmetrical Multiphase Concentrated-Wound Surface-Mount PMSMs to Achieve Maximum Torque Density Under Current Harmonic Injection," IEEE T. Ind. Electron., vol. 65, no. 2, pp. 1751-1761. 2018.

[5] N. Bianchi, L. Alberti, and M. Barcaro, "Design and Tests of a Four-Layer Fractional-Slot Interior Permanent-Magnet Motor," IEEE T. Ind. Appl., vol. 52, no. 3, pp. 2234-2240. 2016.

[6] S. Zhu, T. Cox, Z. Xu, and C. Gerada, "Novel 24-slots14-poles fractional - slot concentrated winding topology with low - space harmonics for electrical machine," The Journal of Engineering, vol. 2019, no. 17, pp. 3784-3788. 2019.

[7] Y. Demir and M. Aydin, "Design, analysis and validation of a dual three-phase 72-slot, 12-pole permanent magnet synchronous motor,", IEEE, 2016, pp. 1598-1603.

[8] Y. Yang, M. M. Rahman, T. Lambert, B. Bilgin, and A. Emadi, "Development of an External Rotor V-Shape Permanent Magnet Machine for E-Bike Application," IEEE T. Energy Conver., vol. 33, no. 4, pp. 1650-1658. 2018.

[9] S. Xiao et al., "Multi-Objective Pareto Optimization of Electromagnetic Devices Exploiting Kriging With Lipschitzian Optimized Expected Improvement," IEEE T. Magn., vol. 54, no. 3, pp. 1-4. 2018.